PCCP

ROYAL SOCIETY OF CHEMISTRY

PAPER

Cite this: *Phys. Chem. Chem. Phys.*, 2020, **22**, 2351

A guinea pig for conformer selectivity and mechanistic insights into dissociative ionization by photoelectron photoion coincidence: fluorocyclohexane

Xiangkun Wu,[ab] Xiaoguo Zhou,[*b] Patrick Hemberger[a] and Andras Bodi[*a]

We studied fluorocyclohexane ($C_6H_{11}F$, FC6) by double imaging photoelectron photoion coincidence spectroscopy in the 9.90–13.90 eV photon energy range. The photoelectron spectrum can identify species isomer and, in this case, even conformer selectively. *Ab initio* results indicated that the axial conformer has two, close-lying cation electronic states. With the help of Franck–Condon simulations of the vibrational fine structure, we determined the origin of three transitions, (i) axial FC6 → axial $FC6^+$ of C_1 symmetry ($\tilde{\mathbf{X}}^+$, A″ in C_S), (ii) equatorial FC6 → equatorial $FC6^+$ of C_1 symmetry ($\tilde{\mathbf{X}}^+$, A″ in C_S), and (iii) axial FC6 → A′ axial $FC6^+$ of C_S symmetry ($\tilde{\mathbf{A}}^+$) as 10.12 ± 0.01, 10.15 ± 0.01 and 10.15 ± 0.02 eV, respectively. At slightly higher energies, the FC6 cation starts fragmenting by HF loss (E_0 = 10.60 eV), followed by sequential CH_3 (E_0 = 10.71 eV) or C_2H_4 (E_0 = 11.06 eV) loss. Surprisingly, the methyl-loss step has an effective barrier of only 0.11 eV, and yet it is a slow process at threshold. Based on the statistical model, this is explained by isomerization and stabilization of the $C_6H_{10}^+$ intermediate. The highest energy channel observed, vinyl fluoride (C_2H_3F) loss yielding $C_4H_8^+$ appears in the breakdown diagram at 12 eV, which agrees with the computed threshold to cyclobutane cation formation. However, the model predicted a *ca.* 1 eV competitive shift for this parallel channel, *i.e.*, an E_0 = 11.23 eV. This led us to explore the potential energy surface to find a lower-lying fragmentation channel including H-transfer steps. Rate constant measurements and statistical modeling thus yield fundamental insights into the reaction mechanism beyond what is immediately seen in the mass spectra.

Received 15th October 2019,
Accepted 5th January 2020

DOI: 10.1039/c9cp05617c

rsc.li/pccp

1. Introduction

Substituted cyclohexane diastereomers are a common textbook example of conformational behavior.[1] By far the most stable cyclohexane conformer is the chair, which exhibits the least steric repulsion and no angular strain. In monosubstituted cyclohexanes, the chair minimum splits into two distinctly different stable diastereomers, as the ligand may assume an equatorial (e-) or an axial (a-) orientation with respect to the cyclohexane ring. In most cases, the axial conformer is less stable because of 1,3-*syn*-diaxial repulsive interaction between the bulky substituent and the axial hydrogens at C3 and C5. Steric effects were questioned as the sole driving force for equatorial preference, when the axial conformer was found to be dominant in 1-trifluoromethyl-1-silacyclohexane.[2] Theoretical works attempted to rationalize the surprising axial preference of numerous, partly quite bulky ligands in cyclohexane and its analogues.[3,4] Experimental works, most notably, low-temperature NMR, gas electron diffraction and temperature-dependent Raman spectroscopy studies continue to unveil details of the conformational properties of substituted cyclohexane analogues.[5,6] Photoelectron spectroscopy and dissociative photoionization studies on monohalogenated silacyclohexanes revealed trends in the electronic and bonding structure as a function of halogen size.[7] The Si–X bond is stronger than the C–X bond and, as a result, only iodosilacyclohexane loses halogen-containing neutral fragments upon dissociative ionization. Mass spectra of halocyclohexanes suggest that hydrogen halogenide or halogen atom loss is the first step in the fragmentation of the parent ion.

Fluorocyclohexane (FC6) is a monosubstituted cyclohexane and its conformational behavior has been studied by electron diffraction,[8] NMR spectroscopy,[9–14] microwave spectroscopy,[15,16] and IR spectroscopy.[17–19] The conformational equilibrium was also investigated computationally,[20,21] complemented by experimental methodologies.[22] These studies showed that the

[a] *Laboratory for Synchrotron Radiation and Femtochemistry, Paul Scherrer Institute, 5232 Villigen, Switzerland. E-mail: andras.boedi@psi.ch*

[b] *Hefei National Laboratory for Physical Sciences at the Microscale, Department of Chemical Physics, University of Science and Technology of China, Hefei 230026, China. E-mail: xzhou@ustc.edu.cn*

equatorial conformer (e-FC6) is more stable than the axial a-FC6 by 0.6–1.1 kJ mol^{-1} and the inversion energy between the two is 40–45 kJ mol^{-1}. This means that the abundance of the axial isomer is approximately 40–45% at room temperature in the gas phase. As reported in the literature[23] and confirmed by our preliminary calculations, the ambient interconversion rate between the two is on the order of 10^5 s^{-1}, meaning that thermal equilibrium is reached within a few μs.

Photoelectron photoion coincidence (PEPICO) spectroscopy, combined with tunable vacuum ultraviolet (VUV) synchrotron radiation,[24–26] has yielded insights with unprecedented detail into dissociative photoionization mechanisms and energetics.[27,28] It has revealed the role of electronic state in fragmentation of small halogenated molecules,[29] unveiled complex dissociation mechanisms with parallel and sequential steps,[30] provided chemical insights into the effect of remote double bonds on reactivity,[31] and delivered accurate thermochemistry and energetics of elusive species.[32,33] PEPICO affords a very detailed view into photoionization thanks to its multiplexing advantages[34] and can even support *ab initio* simulation of mass spectra.[35,36] By tuning the photon energy and analyzing the electron kinetic energy, the internal energy deposited in the parent ion is set and internal energy selection is achieved. By virtue of coincident photoion TOF analysis, photoion mass selected photoelectron spectra can also be plotted, which has proven to be an isomer selective analytical tool in the analysis of reactive mixtures.[37]

Isobaric species and constitutional isomers of a given stoichiometric formula may have significantly different ionization energies, which allows for their isomer-selective detection solely by photoionization mass spectrometry using tunable VUV radiation.[38,39] However, recording the photoelectron spectrum and modeling the vibrational progressions by Franck–Condon calculations is often advantageous to identify species isomer selectively when their structure it is not *a priori* known.[40] Diastereomers exhibit slightly different spectral signatures, which can typically only be resolved using high-resolution techniques, *e.g.*, ZEKE.[41] Nonetheless, threshold photoelectron spectra (TPES) indicated the presence of both diastereomers, *trans* and *cis*, of the 1-methylallyl radical in pyrolysis[42] and combustion[43] environments. Such insights are worthwhile, because, for example, catalytic semihydrogenation is a promising technique to yield alkenes from alkynes[44] and the key to diastereomeric selectivity may lie with the reactive intermediates involved. Preliminary calculations indicated that the ionization energies of the axial and equatorial FC6 conformers differ by a few tens of meV. Going one step further, the first motivation of this work is to show if conformational isomers can also be distinguished based on their slightly different photoelectron spectrum at room temperature.

The fractional abundance of the parent and fragment ions is plotted in the breakdown diagram as a function of photon energy. If the parent ion is metastable close to the dissociative photoionization threshold and the acceleration region is long enough in the mass spectrometer, slow dissociation rate constants in 10^3–10^7 s^{-1} range result in asymmetrical fragment ion peak shapes and can be extracted based on the ion optics parameters.[45] Both the kinetic and the competitive shift can be modelled in a statistical framework.[46] The former originates from that fact that a certain amount of excess energy is required above the thermochemical threshold to raise the dissociation rate constant high enough so that fragmentation can take place quantitatively on the time scale of the experiment. The latter is caused by a fast competing parallel channel with a lower-lying threshold, which delays the appearance of the fragment ion of interest as its formation rate has to be commensurate within the dynamic range of the experiment with that of the lower-lying channel.

In the light of recent results on halosilacyclohexanes,[7] it is interesting to establish the dissociative photoionization mechanism of fluorocyclohexane quantitatively, compare it with that of fluorosilacyclohexane and discuss the chemical changes induced by substituting a carbon for silicon. Our second motivation is therefore to record and model the breakdown diagram and establish the fragmentation mechanism and its driving forces in ionized fluorocyclohexane.

2. Experimental and computational

Experiments were performed at the VUV beamline of the Swiss Light Source, Paul Scherrer Institute. The details of the beamline and the double imaging Photoelectron Photoion Coincidence (CRF-PEPICO) spectrometer have been described elsewhere,[47,48] and the setup is only outlined here. VUV synchrotron radiation was generated by a bending magnet, collimated, dispersed by a grazing incidence monochromator with a 600 lines per mm laminar grating and focused at a 200 μm exit slit in a gas filter at an energy resolution of 2 meV at 8 eV. The gas filter was filled with a mixture of neon, argon and krypton at a pressure of 10 mbar over an optical length of 10 cm to suppress higher-order radiation above 14 eV. The absolute photon energy was calibrated using autoionization lines of argon in the first and second order.

Fluorocyclohexane (Sigma-Aldrich, 97%) was kept at room temperature and seeded into the ionization chamber through a needle valve. In the interaction region, the VUV beam intersects the effusive beam and ionizes the sample. Electrons and ions are extracted in opposite directions by a constant, 125 V cm^{-1}, electric field. Position-sensitive delay-line anode detectors (Roentdek, DLD40) detect electrons and ions in velocity map imaging conditions as well as space focusing conditions for the latter at the end of the two flight tubes in the spectrometer. Threshold electrons with less than 2 meV kinetic energy are projected onto the central spot of the detector and so are kinetic energy electrons without an off-axis momentum component. The resultant hot electron contamination of the threshold signal was subtracted based on the signal in a small ring around the center spot as proposed by Sztáray and Baer.[49] As the electron TOF is negligible relative to the ion TOF, electron hits are used as the start signal for the ion TOF analysis.[50] The experimental data yield the TPES and the photoion mass-selected threshold photoelectron spectra (ms-TPES) of the parent and daughter ions. They are used to plot the breakdown diagram, which is modelled

simultaneously with the time-of-flight distributions for metastable dissociations.

The statistical modeling approach to dissociative photoionization was described previously,[46] and only key aspects are emphasized here. The internal energy of the parent ion is determined by the thermal energy of the neutral, the photon energy, and the adiabatic ionization energy. In fast dissociations without competing processes, the integral of the internal energy distribution above the barrier yields the abundance of the fragment ion. If the parent ion is metastable or if competing fragmentation processes are open at the same energy, the density of states of the parent ion and the number of states of transition state are used to calculate the unimolecular dissociation rate constant, according to the RRKM theory as:[51–53]

$$k(E) = \frac{\sigma \cdot N^{\ddagger}(E - E_0)}{h \cdot \rho(E)}, \quad (1)$$

where $N^{\ddagger}(E - E_0)$ is the number of states of transition state at the excess energy, $E - E_0$, above the dissociation barrier, E_0 is the 0 K appearance energy, $\rho(E)$ is the density of states of the dissociating ion, h is Planck's constant, and σ corresponds to the symmetry of the reaction coordinate. The appearance energy is an adjustable parameter and the lowest five vibrational frequencies of the transition state are scaled by a common, fitted factor to reproduce the experimental data. In order to obtain the internal energy distribution of the fragment ion available in sequential dissociation processes, the excess energy is partitioned statistically between the fragment ion, the leaving neutral and the newly formed rotational and translational degrees of freedom without adjustable parameters.

Computed vibrational frequencies, rotational constants and appearance energies are used to construct the initial statistical model. To provide this input, all reactants, products, intermediates and transition states were located on the ground state potential energy surface of FC6 cations using density functional theory at the B3LYP/6-311+G(d,p) level. The energies of the stationary points were further refined using Gaussian-4 (G4) theory[54] using the Gaussian 16 A.03 program package.[55] Franck–Condon simulations were carried out by calculating the nuclear wave function overlap between the neutral molecule and the cation at room temperature within the double harmonic approximation. The vibrational fine structure of the first TPES band was then fitted by shifting the origin of the FC simulations to identify ionization energies. In addition, geometry optimizations and electronic energy calculations were carried out at the EOM-IP-CCSD/6-311G(d) and EOM-IP-CCSD/cc-pVTZ levels of theory, respectively, using Q-Chem 4.3.[56]

3. Results and discussion

3.1. Threshold photoelectron spectrum

The TPES of FC6 was recorded in the 9.90–11.30 eV photon energy range using a step size of 4 meV and in the 11.30–13.90 eV range using a 10 meV step size. As shown in Fig. 1(a), there is distinct vibrational fine structure at the beginning followed by several structureless bands. Neutral axial and equatorial FC6 conformers are nearly isoenergetic and present in close to equal abundance. Hence, both of them contribute to the TPES during photoionization. The neutral a-FC6 and e-FC6 conformers are of C_S symmetry, both with a″ and a′ highest occupied molecular orbital (HOMO) and HOMO−1, respectively (Fig. 1(b)). EOM-IP-CCSD calculations confirmed that the ground cation state is of A″ symmetry in C_S, meaning that it indeed corresponds to removing an electron from the HOMO. However, said C_S structure is a transition state in the $\tilde{X}^+$ state in both conformers, which relaxes by stretching the C1–C2 bond into an asymmetric, C_1 structure. In the equatorial conformer, the vertical ionization energy to the $\tilde{A}^+$ A′ state lies *ca.* 0.3 eV higher than the one to the ground A″ cation state, but the two ionization energies are nearly equal in the axial conformer. This near-degeneracy, however, does not affect the validity of the EOM-IP-CCSD calculations shown in Fig. 1, because the two states are of different symmetry. This striking difference between the conformers can be rationalized in terms of the a′ HOMO−1 orbital being more stabilized in the equatorial conformer as it has a more pronounced bonding character. This is best seen at the C–H bonds between the axial hydrogens at the vicinal carbons to the C–F group (C2 and C6) in the axial and equatorial isomer in

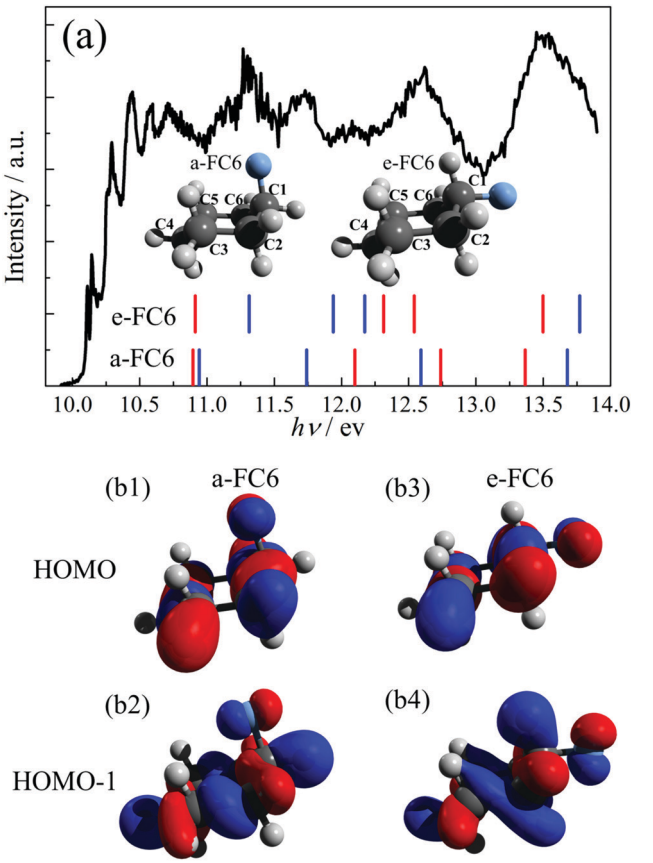

Fig. 1 (a) Threshold photoelectron spectrum of fluorocyclohexane in the energy range of 9.90–13.90 eV. The sticks show the vertical ionization energies calculated at the EOM-IP-CCSD/cc-pVTZ level for e-FC6 (upper level) and a-FC6 (lower level). Red and blue sticks indicate A″ and A′ states, respectively. (b1) and (b2) are the HOMO and HOMO−1 orbitals for a-FC6, (b3) and (b4) are the HOMO and HOMO−1 orbitals for e-FC6, respectively.

Fig. 1(b2 and b4). When the geometry of the originally A″ a-FC6$^+$ state is optimized in C_1 symmetry, the energy relaxes by 0.6 eV and the near degeneracy of the two states is lifted, as the 1st (originally A′) excited state lies 2 eV higher in energy. The A′ a-FC6$^+$ excited state geometry optimization preserves the symmetry and relaxes by C–F bond elongation to an energy *ca.* 30 meV higher than the ground, originally A″ state. However, at this geometry, the A″ state lies almost 1.5 eV higher in energy than the A′ state. Thus, both states are the lowest energy ones at the respective optimized geometries by a significant margin, and ground-state calculations can be applied to address them without noteworthy spin contamination of the unrestricted wave function.

Before discussing Franck–Condon simulations, we would like to point out a few aspects why these findings are peculiar. First, the quasi-degeneracy of the first two states is unique to the axial fluorocyclohexane cation, compared to an experimentally seen and computationally confirmed splitting of *ca.* 0.7 eV in 1-fluorosilacyclohexane.[7] Second, the fact that two electronic states are available close to the ionization onset of the axial conformer and only one in the equatorial one means that, everything else being constant, the ionization cross section of the axial conformer is expected to be *ca.* double that of the equatorial conformer, depending on the photoionization efficiency. Absolute photoionization cross sections are much sought after measurables to quantify absolute concentrations using photoionization mass spectrometry, and experimental[57] and theoretical[58] efforts have been invested in determining them accurately. However, they might not be perfectly transferable quantities between experiments when they depend on the molecular orientation strongly[59] or, as is seen here, low-lying excited states enhance them conformation dependently. Third, it is intriguing that the axial and equatorial conformers are almost isoenergetic in the neutral and cation states, meaning that one is tempted to look for highly resolved IR, microwave or NMR signatures to tell them apart conclusively. However, underneath the apparent equivalence, there is a sizeable, 300 meV difference between the excitation energy to the first excited electronic state of the axial and the equatorial cations and further, quite fundamental differences in the higher ionization energies, as well.

After the rising edge if the TPES, there is an almost constant signal up to 14 eV. This is surprising and hints at overlapping electronic and vibrational transitions. As detailed modeling the spectrum of such a broad and congested energy range is not within reach, we carried out EOM-IP-CCSD calculations at the neutral geometries to predict the vertical transitions, which indicate the approximate energy of the maximum of the corresponding TPES band. These are indeed spread out and the slight drop in intensity at around 13 eV is also quite well reproduced by the absence of vertical transitions in this energy range. Most of the spectral information is, however, contained in the rising edge of the TPES, which exhibits a vibrational fine structure, which is why we focused on modeling the low-energy part of TPES, considering three ionizing transitions: e-FC6 → e-FC6$^+$ ($\tilde{\mathbf{X}}^+$, C_1), a-FC6 → a-FC6$^+$ ($\tilde{\mathbf{X}}^+$, C_1), and a-FC6 → a-FC6$^+$ ($\tilde{\mathbf{A}}^+$ ^{2}A′, C_S).

The Franck–Condon simulated spectra at the B3LYP/6-311+G(d,p) level of theory at a temperature of 298 K were convoluted with a Gaussian of 100 cm^{-1} full width at half-maximum (FWHM) to account for the rotational envelope for each of these transitions and are shown in Fig. 2. The spectrum could not be satisfyingly reproduced assuming only one axial transition. Instead, assuming the equal axial and equatorial populations as well as equal absolute contribution of the three transitions considered, the overall simulated spectrum was obtained as the direct sum of the three components, and only the origins were shifted to obtain the best fit with the experimental spectrum.

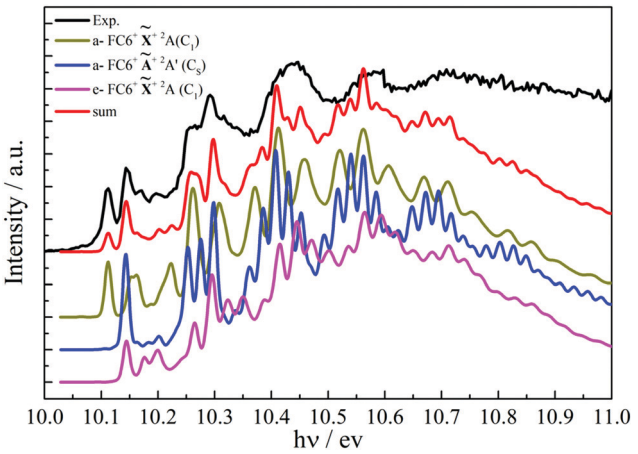

Fig. 2 TPE spectrum of fluorocyclohexane in the ground ionic band, together with the Franck–Condon simulation of the one equatorial and two axial states.

As shown in Fig. 2, the transition of a-FC6 (C_S) → a-FC6$^+$ ($\tilde{\mathbf{X}}^+$, C_1) has the lowest band origin at 10.11 ± 0.01 eV, while the other two transitions e-FC6 (C_S) → e-FC6$^+$ ($\tilde{\mathbf{X}}^+$, C_1) and a-FC6 (C_S) → a-FC6$^+$ ($\tilde{\mathbf{A}}^+$, C_S) have the almost identical band origin at 10.14 eV. Taking into account the Stark shift of 8 meV at the constant 125 V cm^{-1} extraction field,[60] the adiabatic ionization energies to these final states are 10.12 ± 0.01, 10.15 ± 0.01 and 10.15 ± 0.02 eV, respectively. These values are in serendipitous agreement with the G4-calculated ionization energies of 10.12, 10.15 and 10.15 eV, respectively.

3.2. Threshold ionization mass spectra

Threshold photoionization TOF mass spectra were recorded in the 9.90–13.90 eV photon energy range. Fig. 3(a) shows six representative TOF distributions with fragment ion peaks at *m*/*z* 82, 74, 73, 69, 67, 56, 55, 54, 43, 42 and 41. The parent ion at *m*/*z* 102 was only observed below 10.6 eV in threshold photoionization. HF loss yields the fragment ion at *m*/*z* 82 in the lowest energy dissociation channel, which appeared gradually as the photon energy was increased. The parent ion disappears from the breakdown diagram within 0.6 eV of the ionization energy. Despite the shallow potential energy well, the HF-loss daughter ion peak exhibits a slight asymmetry (see at $h\nu$ = 10.45 eV in Fig. 3(a)), which indicates a tight transition state. The C–F bond energy is much higher than that of C–Cl or C–Br bonds.[7] This explains why, in contrast with chlorocyclohexane and bromocyclohexane,[61] no direct halogen loss could be observed

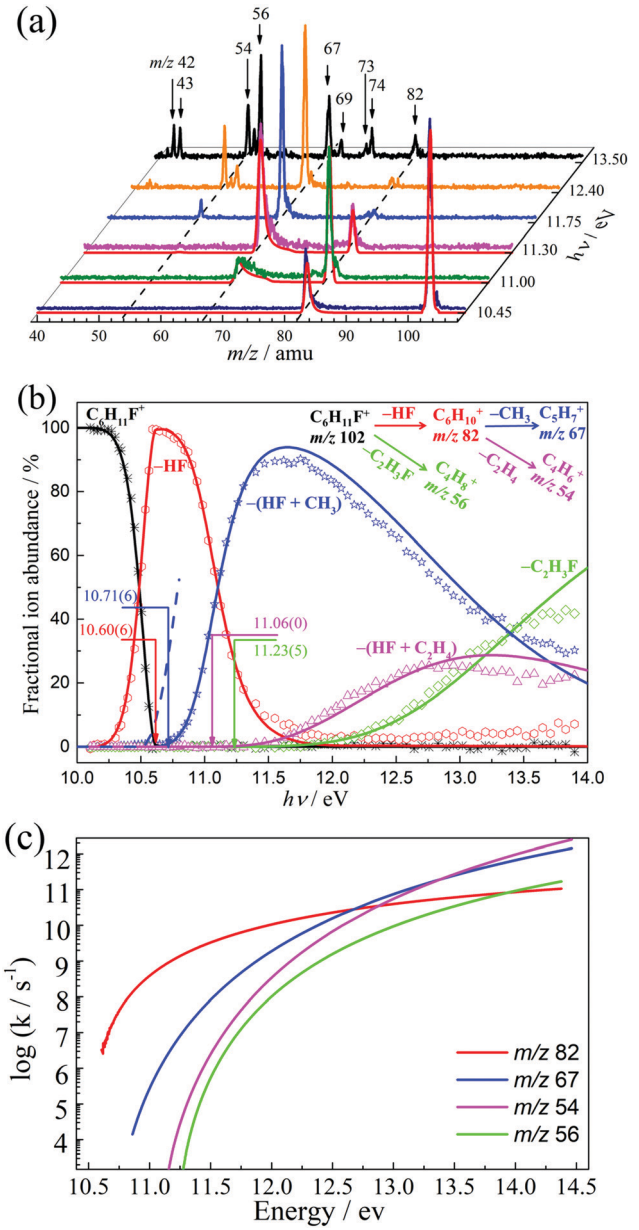

Fig. 3 (a) Threshold photoionization mass spectra of FC6 at representative photon energies. (b) Breakdown diagram of dissociative photoionization of fluorocyclohexane in the energy range of 9.90–13.90 eV. Open symbols represent the experimental fractional abundances, and the solid lines show the simulated results with the statistical model. The 0 K appearance energies of the major fragment ions were determined and noted with the arrows. The blue dashed line shows the *m/z* 67 breakdown curve as a fast dissociation without a kinetic shift. (c) The model dissociation rate constant curves from the respective precursors (see text) as a function of energy above the neutral. The experiment yields absolute rate information for methyl loss (blue) and, to a limited degree, HF loss (red). Relative rate information is contained in the breakdown diagram for the parallel processes vinyl fluoride loss (green) and ethylene loss (violet).

in fluorocyclohexane. Fluorinated hydrocarbons have been shown to exhibit isolated state behavior and non-statistical fluorine atom loss at higher energies,[62] but no such channel was found in fluorocyclohexane, either. The second fragment ion peak at *m/z* 67 ($C_5H_7^+$, HF + CH_3 loss) was observed above 10.6 eV. As seen at $h\nu$ = 11.00 eV in Fig. 3(a), this slow, sequential dissociation step from the HF fragment ion exhibits a highly asymmetric TOF profile at low energies. Here again, the low CH_3-loss dissociation rates together with apparently shallow potential energy well of the HF-loss fragment suggest a tight transition state, at least at first glance.

As the photon energy was increased, further fragment ions appeared as seen in Fig. 3(a). Besides *m/z* 67 and 82, the fragment ions *m/z* 54 and 56 were observed with considerable intensity above 11.3 eV. Additional fragment ions appeared at even higher energies, $h\nu$ > 12.5 eV, at *m/z* 74, 73, 69, 55, 43, 42 and 41 with small (<10%) abundances. The *m/z* 74, 73 and 69 fragment ions may be produced by the loss of C_2H_4, C_2H_5, and CH_2F from the parent FC6$^+$ ion, respectively. The less intense *m/z* 55 fragment ion appeared almost at the same photon energy as the *m/z* 56 one, with an abundance following that of *m/z* 56 ion. Thus, it is possible that the two processes share the same rate determining transition state and a later H-transfer step is responsible for the small branching ratio towards the *m/z* 55 fragment ion. The experimental data for the highest-energy fragment ions *m/z* 43, 42, and 41, are insufficient to propose a conclusive dissociation mechanism.

The fractional ion abundances belonging to the dominant fragmentation pathways from the parent *m/z* 102 to the *m/z* 82, 67, 56, and 54 daughter ions are plotted in the breakdown diagram in Fig. 3(b). It is interesting that, although the abundance of the HF-loss product $C_6H_{10}^+$ (*m/z* 82) decreases as sequential methyl loss opens up, it starts slowly rising again after 12.5 eV. This is indicative of further HF-loss pathways from FC6$^+$, which may involve larger kinetic energy release, which in turn stabilizes the fragment ion, as will be discussed later.

Based on the broad crossover region and slowly changing abundances, the *m/z* 54, 56, and 67 breakdown curves in Fig. 3(b) correspond to slowly changing rate constant ratios and, hence, to competing fragmentation channels. There are two candidate pathways to yield the *m/z* 54 and 56 ions. One is the direct C_2H_5F and C_2H_3F loss from the FC6$^+$ parent ion ($C_6H_{11}F$, *m/z* 102) and the other is the sequential dissociation of the HF-loss fragment ion *m/z* 82 by C_2H_4 and C_2H_2 loss, respectively. As seen in the electron ionization mass spectra of the C_6H_{10} isomers in the NIST Chemistry Webbook,[63] the *m/z* 54 is a major $C_6H_{10}^+$ fragment, but the fragment ion at *m/z* 56 is not to be seen. Therefore, and as confirmed by calculations below, *m/z* 56 ions are a direct fragment of FC6$^+$ by C_2H_3F loss, while *m/z* 54 ions are a parallel dissociation fragment from *m/z* 82 by C_2H_4 loss.

3.3. Initial decomposition pathways of FC6$^+$

The dissociation steps deduced from the breakdown diagram suggest that, similar to 1-halogenated silacyclohexanes,[7] complicated isomerization and decomposition pathways are involved in the fragmentation of energetic FC6$^+$ cations. C_2H_3F loss yielding *m/z* 56 could conceivably take place by two consecutive C–C bond breaking steps in the six-membered ring, but even this process would have to conclude by C–C bond formation as the cyclobutane

cation is formed. Thus, the potential energy surface of the parent and intermediate fragment ions has to be explored to find the viable and energetically allowed reaction coordinates using constrained optimizations scanning bond lengths and angles.

The $FC6^+$ cation also has two conformers, a-$FC6^+$ and e-$FC6^+$, at a very small energy difference, ≈30 meV, in the ground state. The first excited state of a-$FC6^+$ is isoenergetic with the ground state e-$FC6^+$ and is also the lowest energy state at its optimized geometry. Assuming that the isomerization barrier between the two is comparable to that in the neutral, the interconversion rate constant between axial and equatorial conformers is expected to be 10^5 s^{-1} already at room temperature at the adiabatic ionization energy.[23] Internal conversion between the ground and first excited states in the axial conformer is probably even faster. We have explored alternative fragmentation paths, and, for the sake of simplicity, will be reporting the lowest-lying transition states and using e-$FC6^+$ cation as parent ion to discuss dissociation mechanism here. This is appropriate as medium-sized cations normally dissociate statistically, unless repulsive or isolated states are involved,[27,29] and the phase space is dominated by the lowest-energy electronic state even when the excitation energies are moderate.

Fig. 4 displays the fragmentation pathways from the $FC6^+$ cation, leading to the *m*/*z* 82 and 56 ions. Direct C–H [**13**] and C–F [**12**] bond fission channels are also shown for comparison at barrier heights of 0.95 and 1.90 eV, respectively. The lowest energy fragmentation channel to $C_6H_{10}^+$ + HF goes over a transition state at a much lower barrier height of 0.36 eV. Fluorine atom loss never becomes competitive and hydrogen atom loss is never seen because fluorine will "grab" the leaving hydrogen before enough kinetic energy can be accumulated in the direct H-loss reaction coordinate. Thus, direct bond breaking products cannot be observed. Tight and energetic three- and four-membered ring transition states are associated with H abstraction by fluorine from the geminal (α-, C1) and the vicinal (β-, C2 and C6) carbon. Thus, the β-hydrogen is not lost from C2 and the cyclohexene cation is not an immediate product of HF loss. As shown in Fig. 4, H-abstraction from the δ position (C4) can form the *m*/*z* 82 ion [**3**] and HF molecule *via* the transition state [**2**]‡ at 0.36 eV. Similarly, the *m*/*z* 82 ion isomer [**5**] is calculated to be more stable by 0.19 eV than [**3**], and can be produced by H-abstraction from the γ position (C3) over a higher-lying transition state [**4**]‡ at 0.64 eV. The isomerization path connecting these two HF-loss products and further, more stable $C_6H_{10}^+$ isomers will be discussed later.

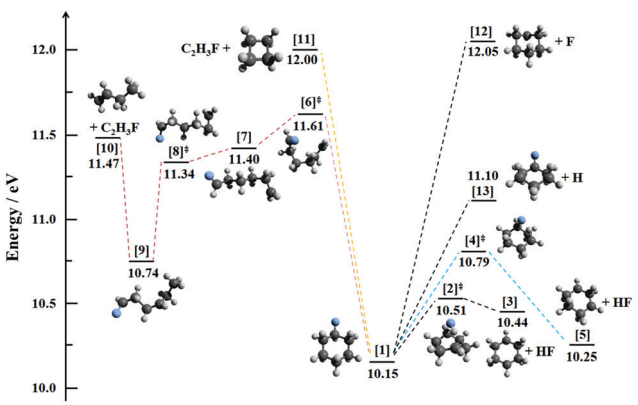

Fig. 4 The initial fragmentation pathways of fluorocyclohexane cation to produce the fragment ions of *m*/*z* 82 and 56, as well as the direct C–F and C–H bond fissions, where the energies relative to e-FC6 are evaluated with the G4 composite method.

As established above, *m*/*z* 56 by C_2H_3F loss is a fragmentation product of the parent ion [**1**] along with *m*/*z* 82 by HF loss. Two pathways are shown from the e-$FC6^+$ cation in Fig. 4. The conceptually simple direct C–C bond fissions in the cyclohexane ring to yield the cyclobutane ion [**11**] and C_2H_3F requires 12.00 eV. Although this energy coincides with the appearance of *m*/*z* 56 in the breakdown diagram, the statistical model (see below) indicated a significant competitive shift. Indeed, upon careful observation, the *m*/*z* 56 fragment ion signal rises slowly already at 11.75 eV. This led us to further explore the potential energy surface in search for a lower-lying dissociation channel. Hydrogen transfer barriers over the intact six-membered $FC6^+$ ring between carbon atoms require at least 11.89 eV, which is higher than the HF formation transition state or the ring-opening barrier. Therefore, processes competing with HF loss will start with ring opening, which may be followed by hydrogen transfers in the resulting, more floppy carbon chain. Transition state [**6**]‡ has been found to yield the *m*/*z* 56 fragment ion at already 11.61 eV. The ring-opening intermediate [**7**] undergoes H-transfer from a CH_2 group to the terminal carbon atom over transition state [**8**]‡ at 11.34 eV. While it has no bearing on the mechanism here, we would like to point out that the transition state [**8**]‡, located in the B3LYP/6-31G(2df,p) geometry optimization step, evaluates to a lower energy than the precursor [**7**]. Such small energy differences at a more advanced level of theory than that of the geometry optimization may be indicative of a flat portion of the potential energy surface.[64,65] The next intermediate, [**9**] at 10.74 eV, can lose C_2H_3F to yield the 1-butene *m*/*z* 56 ion [**10**]. Although this bond fission is strongly endothermic, the activation energy is still lower than the barrier of ring opening. In fact, it is likely that the other H-transfer isomers of *m*/*z* 56, *i.e.*, *cis*-2-butene and *trans*-2-butene may also be produced from [**9**] over the same rate-determining barrier at transition state [**6**]‡.

3.4. Sequential dissociation pathways from *m*/*z* 82

With the increasing photon energy, the HF-loss fragment ions at *m*/*z* 82, [**3**] and [**5**], may become energetic enough to undergo sequential dissociation. From Fig. 5, the methyl-loss product at *m*/*z* 67, [**17**], can form through a series of hydrogen transfer and ring contraction processes at 10.70 eV. Our calculations confirmed the reaction coordinate from [**5**] to [**17**] as proposed by Bouchoux *et al.* for the dissociation of cationic cyclohexene.[66] The submerged transition states are not expected to limit the dissociation rate and the appearance energy of [**17**] is determined by its energy. However, the system passes the low-lying intermediate [**16**] along the reaction coordinate. As confirmed by the statistical model (see below), this explains the kinetic shift observed in sequential methyl loss, as the effective potential energy well is more than 1.5 eV deep, increasing the

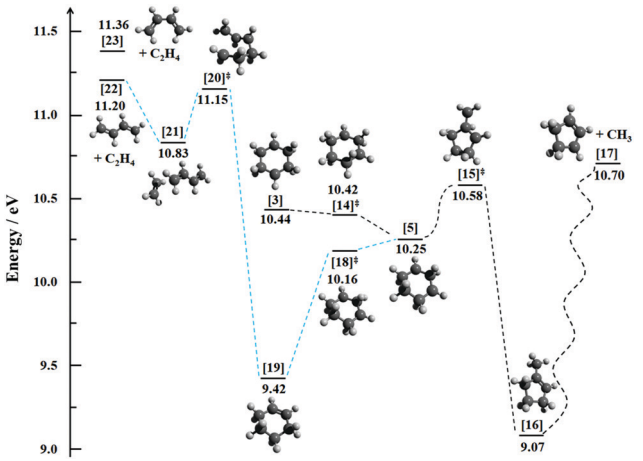

Fig. 5 The sequential dissociation pathways of the *m*/*z* 82 ion to produce the fragment ions of *m*/*z* 67 and 54. Low-lying intermediates for [**5**] → [**15**]‡ and [**16**] → [**17**] are skipped for clarity. The energies of intermediates and transition states are calculated using the G4 composite method, relative to the equatorial conformer of neutral fluorocyclohexane.

density of states of the reactant and thereby lowering the dissociation rate (see eqn (1)). In fact, the slow dissociation rates are proof that the system explores the phase space and intramolecular vibrational relaxation (IVR) takes place in the [**16**] potential energy well instead of bypassing it and proceeding directly to [**17**].

Another sequential fragment of the *m*/*z* 82 daughter ion $C_6H_{10}^+$ is the *m*/*z* 54 fragment ion by sequential ethylene loss (28 amu). Although the cyclohexene cation [**19**] is not a direct fragmentation product of the parent ion, both direct products [**3**] and [**5**] can readily isomerize and yield [**19**] at 9.42 eV. Bouchoux *et al.* suggested that the cyclohexene ion undergoes a retro-Diels–Alder reaction to yield *cis*-1,3-butadiene cation [**23**] (*m*/*z* 54),[66] for which we calculated a dissociative photoionization energy of 11.36 eV using G4. We have also found a lower-lying dissociation pathway yielding the more stable *trans*-1,3-butadiene cation [**22**] at 11.20 eV after surmounting the submerged ring opening transition state [**20**]‡ at 11.15 eV and passing the intermediate minimum [**21**] at 10.83 eV.

The region of the [**3**] → [**14**]‡ → [**5**] → [**18**]‡ → [**19**] path is poorly represented on the potential energy surface in Fig. 5. The G4 energies for the isomerization of the immediate HF-loss products to the deep-well minimum cyclobutene from [**3**] are monotonically downhill despite two transition states along the way. In contrast to [**7**] → [**8**]‡ → [**9**] (Fig. 4) or previously discussed slightly too low energy transition states,[64,65] the almost 100 meV drop in energy for [**5**] → [**18**]‡ indicates more than just a "flat" part of the potential. In addition to B3LYP, we used the M06-2X and ωB97-XD functionals with the def2-TZVPP basis set and the Synchronous Transit-Guided Quasi-Newton (STQN) method[67] to explore these interconversion paths. These methods predict a monotonously downhill path from [**5**] to [**19**], but some predict a barrier for [**3**] → [**14**]‡ → [**5**]. The most trustworthy, although not fully converged, pathway was determined using coupled cluster singles and doubles, CCSD/6-311++G(d,p). This predicts [**5**] to be a minimum at 10.50 eV (G4 single-point energy referenced to [**19**] without zero-point energy), which forms [**3**]‡ at 10.53 eV, which then isomerizes by synchronous H-transfers to [**19**]. However, when the [**3**] structure was further explored, we could find a minimum at 10.51 eV, as well. If static electron correlation is large or if the Born–Oppenheimer approximation does not hold, such *ab initio* tools are insufficient to tackle the six-membered ring isomerization paths on the $C_6H_{10}^+$ potential energy surface. Thanks to the statistical model, we are nevertheless able to determine that (1) the prompt product of HF loss is predominantly a high-energy $C_6H_{10}^+$ isomer and (2) methyl loss proceeds from an equilibrated structure in the [**16**] potential energy well.

3.5. Dissociative photoionization model

Based on the insights gained by exploring by potential energy surface, as guided by the breakdown diagram, we set up a statistical model to determine the experimental 0 K appearance energies, *i.e.*, the dissociative photoionization reaction energies when the fragmentation is energetically allowed at the product energies and the activation energies otherwise.[46] The lowest-energy decomposition channel is the loss of a HF molecule from $FC6^+$, and the 0 K appearance energy of the *m*/*z* 82 ion is determined as 10.60 ± 0.06 eV (Fig. 3(b)). This value is consistent with the theoretically predicted activation energy of [**2**]‡ at 10.51 eV. The next major product ion, *m*/*z* 67 is formed by sequential methyl loss, and the fragment ion peak is markedly asymmetric at low photon energies. No physically meaningful statistical model would predict slow dissociation rates when the phase space volume of the reactant was calculated using the energy and vibrational frequencies of the immediate HF-loss products. However, when the density-of-states function, $\rho(E)$, of the dissociating ion (see eqn (1)) was based on the deep-well intermediate [**16**], the rates as well as the breakdown curves were fitted easily. The experimental $E_0(C_5H_7^+)$ at 10.71 ± 0.06 eV (Fig. 3(b)) is in exact agreement with the calculated value of 10.70 eV (Fig. 5). This confirms that (i) IVR takes place and the system is equilibrated in [**16**] prior to methyl loss and, (ii) since the width of the breakdown diagram is well reproduced by the statistical model, the kinetic energy release in the HF-loss step is very close to being statistical.[36] Thus, we can rule out that the most stable HF-loss $C_6H_{10}^+$ isomers [**16**] and [**19**] are direct products of HF loss after the system passes a large reverse barrier. However, the rebounding *m*/*z* 82 signal at high photon energies may indicate that a small fraction of HF loss proceeds directly to these and is accompanied by suprastatistical kinetic energy release.

Above 11.25 eV, the *m*/*z* 56 and 54 fragment ions appear as products of C_2H_3F loss from $FC6^+$ and C_2H_4 loss from the HF-loss fragment ion, $C_6H_{10}^+$ (*m*/*z* 82), respectively. As a competitive channel of dissociation of $FC6^+$, the *m*/*z* 56 ion intensity rises very slowly near threshold, indicating a large competitive shift. The rate information for HF loss is poorly constrained because the $FC6^+$ parent ion is only very slightly metastable. The rise of *m*/*z* 56 is determined by the rate constant ratios and is extrapolated to $E_0(C_4H_8^+)$ = 11.23 ± 0.1 eV, which is

significantly lower than the calculated value of 11.61 eV. A possible reason for this discrepancy may be that the HF-loss rates rise less steeply than predicted by the statistical model.

The 1,3-butadiene ion (*m*/*z* 54) is also formed in a parallel process in a sequential dissociation of the *m*/*z* 82 ion. Our calculations indicate that it is not the direct *cis* product of a retro-Diels–Alder reaction but corresponds to the *trans* isomer produced *via* an isomerization process. The appearance threshold of $E_0(C_4H_6^+)$ is determined as 11.06 ± 0.1 eV in experiment, which is moderately lower than the calculated value, 11.20 eV, indicating again that the RRKM model may overestimate the competitive shift, possibly for similar reasons as it was found to overestimate kinetic shifts.[68]

When the α-carbon C1 is exchanged for silicon in 1-fluorosilacyclohexane, it not only lifts the quasidegeneracy of the first ion electronic states (see above), but it also has a profound effect on the dissociative photoionization mechanism.[7] The silicon-containing fragment holds the positive charge and, thanks to the strong Si–F bond, it keeps the fluorine bound, too. The dominant fragmentation channel of $C_5H_{11}SiF^+$ is C_2H_4 loss, which is conceptually similar to the weaker, parallel C_2H_3F loss observed in $C_6H_{11}F^+$. However, ethylene loss from the silicon-containing ring takes place after ring opening over a η^2-bonded intermediate, in which the silicon forms a three-centered bond with the leaving ethylene molecule. The carbonaceous analogue would suffer from angular strain, and, instead, vinyl fluoride is lost after ring opening and H-transfer steps, which leads to the 1-butene cation. Thus, while the electronic structure of fluorosilacyclohexane is, by and large, similar to that of fluorocyclohexane, the fragmentation processes are fundamentally different.

4. Conclusions

Photoelectron photoion coincidence experiments of FC6 were conducted in the 9.90–13.90 eV photon energy range. Franck–Condon simulations based on DFT calculations and supported by EOM-IP-CCSD results identified the ionization energy for three transitions: (i) a-FC6 (C_S, A′) → a-FC6$^+$ (C_1, A″ in C_S), (ii) e-FC6 (C_S, A′) → e-FC6$^+$ (C_1, A″ in C_S) and (iii) a-FC6 (C_S, A′) → a-FC6$^+$ (C_S, A′) at 10.12 ± 0.01, 10.15 ± 0.01 and 10.15 ± 0.02 eV, respectively. The a′ HOMO−1 in e-FC6 has a more pronounced bonding character than in a-FC6, which explains its stabilization and the large, *ca.* 300 meV difference in the corresponding ionization energy to the $\tilde{A}^+\ ^2A'$ state. Thus, otherwise almost isoenergetic diastereomers may exhibit large energy differences in certain electronic states. Furthermore, the quasi degeneracy of the first two cation states in a-FC6$^+$ means that the ionization cross section of a-FC6 is expected to be *ca.* twice of that of e-FC6, which is a first example of an inferred, strongly conformer-dependent ionization cross section.

The breakdown diagram was analyzed to unveil the dissociative photoionization mechanism, and *ab initio* calculations were carried out to explore the reaction pathways. The FC6$^+$ cation dominantly dissociates by two parallel channels to produce *m*/*z* 82 (HF loss, E_0 = 10.60 eV *vs.* G4 value of 10.51 eV) and *m*/*z* 56 (C_2H_3F loss, E_0 = 11.23 eV *vs.* G4 calculated value of 11.61 eV) fragment ions. From *m*/*z* 82, two sequential dissociation channels lead to *m*/*z* 67 (CH_3 loss E_0 = 10.71 eV *vs.* G4 value of 10.70 eV) and 54 (C_2H_4 loss, E_0 = 11.06 eV *vs.* G4 calculated value of 11.20 eV). The statistical model can only reproduce the *m*/*z* 67 breakdown curve if the density of states of the *m*/*z* 82 intermediate is calculated from the [**16**] minimum. The good fit assuming statistical kinetic energy release indicates that HF-loss directly yields high-energy $C_6H_{10}^+$ isomers, which then isomerize to more stable ones and undergo IVR prior to further dissociation.

Conflicts of interest

There are no conflicts to declare.

Acknowledgements

The experimental work was carried out at the VUV beamline of the Swiss Light Source of the Paul Scherrer Institute. The financial support of the Swiss Federal Office for Energy (BFE Contract No. SI/501269-01) and the National Natural Science Foundation of China (No. 21573210, 21873089 and 21903079) are gratefully acknowledged. The work was also financially supported by the National Key Research and Development Program of China (No. 2016YFF0200502).

References

1 J. McMurry, *Organic Chemistry*, Thomson-Brooks/Cole, Belmont, 2004.
2 G. V. Girichev, N. I. Giricheva, A. Bodi, P. I. Gudnason, S. Jonsdottir, A. Kvaran, I. Arnason and H. Oberhammer, *Chem. – Eur. J.*, 2007, **13**, 1776–1783.
3 A. Bodi, R. Bjornsson and I. Arnason, *J. Mol. Struct.*, 2010, **978**, 14–19.
4 R. Bjornsson and I. Arnason, *Phys. Chem. Chem. Phys.*, 2009, **11**, 8689–8697.
5 S. O. Wallevik, R. Bjornsson, A. Kvaran, S. Jonsdottir, I. Arnason, A. V. Belyakov, T. Kern and K. Hassler, *Organometallics*, 2013, **32**, 6996–7005.
6 S. A. Shlykov, B. V. Puchkov, I. Arnason, S. O. Wallevik, N. I. Giricheva, G. V. Girichev and Y. A. Zhabanov, *J. Mol. Struct.*, 2018, **1154**, 570–578.
7 A. Bodi, K. L. Sigurdardottir, A. Kvaran, R. Bjornsson and I. Arnason, *J. Phys. Chem. A*, 2016, **120**, 9188–9197.
8 P. Andersen, *Acta Chem. Scand.*, 1962, **16**, 2337–2340.
9 F. A. Bovey, E. W. Anderson, F. P. Hood and R. L. Kornegay, *J. Chem. Phys.*, 1964, **40**, 3099–3109.
10 E. L. Eliel and R. J. L. Martin, *J. Am. Chem. Soc.*, 1968, **90**, 689–697.
11 F. R. Jensen, C. H. Bushweller and B. H. Beck, *J. Am. Chem. Soc.*, 1969, **91**, 344–351.
12 P. S. Chu and N. S. True, *J. Phys. Chem.*, 1985, **89**, 5613–5616.
13 R. E. Wasylishen, *Can. J. Chem.*, 1986, **64**, 2094–2095.

14 R. K. Harris, A. Nordon and K. D. Harris, *Magn. Reson. Chem.*, 1999, **37**, 15–24.
15 L. Pierce and J. F. Beecher, *J. Am. Chem. Soc.*, 1966, **88**, 5406–5410.
16 L. H. Scharpen, *J. Am. Chem. Soc.*, 1972, **94**, 3737–3739.
17 D. E. Bugay, C. H. Bushweller, C. T. Danehey Jr, S. Hoogasian, J. A. Blersch and W. R. Leenstra, *J. Phys. Chem.*, 1989, **93**, 3908–3911.
18 J. R. Durig, R. M. Ward, K. G. Nelson and T. K. Gounev, *J. Mol. Struct.*, 2010, **976**, 150–160.
19 A. I. Fishman, W. A. Herrebout and B. J. van der Veken, *J. Phys. Chem. A*, 2002, **106**, 4536–4542.
20 E. Białkowska-Jaworska, M. Jaworski and Z. Kisiel, *J. Mol. Struct.*, 1995, **350**, 247–254.
21 C. A. Stortz, *J. Phys. Org. Chem.*, 2010, **23**, 1173–1186.
22 M. Juanes, N. Vogt, J. Demaison, I. León, A. Lesarri and H. D. Rudolph, *Phys. Chem. Chem. Phys.*, 2017, **19**, 29162–29169.
23 F. R. Jensen and C. H. Bushweller, *J. Am. Chem. Soc.*, 1969, **91**, 3223–3225.
24 X. F. Tang, X. G. Zhou, M. L. Niu, S. L. Liu, J. D. Sun, X. B. Shan, F. Y. Liu and L. S. Sheng, *Rev. Sci. Instrum.*, 2009, **80**, 113101.
25 A. Bodi, P. Hemberger, T. Gerber and B. Sztáray, *Rev. Sci. Instrum.*, 2012, **83**, 083105.
26 G. A. Garcia, B. K. Cunha de Miranda, M. Tia, S. Daly and L. Nahon, *Rev. Sci. Instrum.*, 2013, **84**, 053112.
27 T. Baer and R. P. Tuckett, *Phys. Chem. Chem. Phys.*, 2017, **19**, 9698–9723.
28 X. Wu, X. Tang, X. Zhou and S. Liu, *Chin. J. Chem. Phys.*, 2019, **32**, 11–22.
29 X. Wu, T. Yu, Y. Chen, X. Zhou, S. Liu, X. Dai, F. Liu and L. Sheng, *Phys. Chem. Chem. Phys.*, 2019, **21**, 4998–5005.
30 M. F. Heringa, J. G. Slowik, A. S. Prévôt, U. Baltensperger, P. Hemberger and A. Bodi, *J. Phys. Chem. A*, 2016, **120**, 3397–3405.
31 M. F. Heringa, J. G. Slowik, M. Goldmann, R. Signorell, P. Hemberger and A. Bodi, *ChemPhysChem*, 2017, **18**, 3595–3604.
32 M. Steglich, V. B. Custodis, A. J. Trevitt, G. daSilva, A. Bodi and P. Hemberger, *J. Am. Chem. Soc.*, 2017, **139**, 14348–14351.
33 K. Voronova, K. M. Ervin, K. G. Torma, P. Hemberger, A. Bodi, T. Gerber, D. L. Osborn and B. L. Sztáray, *J. Phys. Chem. Lett.*, 2018, **9**, 534–539.
34 A. Bodi, P. Hemberger, D. L. Osborn and B. L. Sztáray, *J. Phys. Chem. Lett.*, 2013, **4**, 2948–2952.
35 C. A. Bauer and S. Grimme, *J. Phys. Chem. A*, 2016, **120**, 3755–3766.
36 K. Majer, R. Signorell, M. F. Heringa, M. Goldmann, P. Hemberger and A. Bodi, *Chem. – Eur. J.*, 2019, **25**, 14192–14204.
37 P. Hemberger and A. Bodi, *Chimia*, 2018, **72**, 227–232.
38 D. L. Osborn, P. Zou, H. Johnsen, C. C. Hayden, C. A. Taatjes, V. D. Knyazev, S. W. North, D. S. Peterka, M. Ahmed and S. R. Leone, *Rev. Sci. Instrum.*, 2008, **79**, 104103.
39 O. Kostko, B. Bandyopadhyay and M. Ahmed, *Annu. Rev. Phys. Chem.*, 2016, **67**, 19–40.
40 P. Hemberger, V. B. Custodis, A. Bodi, T. Gerber and J. A. van Bokhoven, *Nat. Commun.*, 2017, **8**, 15946.
41 S. Ullrich, G. Tarczay, X. Tong, C. E. Dessent and K. Müller-Dethlefs, *Angew. Chem., Int. Ed.*, 2002, **41**, 166–168.
42 M. Lang, F. Holzmeier, P. Hemberger and I. Fischer, *J. Phys. Chem. A*, 2015, **119**, 3995–4000.
43 D. Krüger, P. Oßwald, M. Köhler, P. Hemberger, T. Bierkandt, Y. Karakaya and T. Kasper, *Combust. Flame*, 2018, **191**, 343–352.
44 R. Chinchilla and C. Najera, *Chem. Rev.*, 2013, **114**, 1783–1826.
45 A. Bodi, T. Baer, N. K. Wells, D. Fakhoury, D. Klecyngier and J. P. Kercher, *Phys. Chem. Chem. Phys.*, 2015, **17**, 28505–28509.
46 B. Sztáray, A. Bodi and T. Baer, *J. Mass Spectrom.*, 2010, **45**, 1233–1245.
47 M. Johnson, A. Bodi, L. Schulz and T. Gerber, *Nucl. Instrum. Methods Phys. Res., Sect. A*, 2009, **610**, 597–603.
48 B. Sztáray, K. Voronova, K. G. Torma, K. J. Covert, A. Bodi, P. Hemberger, T. Gerber and D. L. Osborn, *J. Chem. Phys.*, 2017, **147**, 013944.
49 B. Sztáray and T. Baer, *Rev. Sci. Instrum.*, 2003, **74**, 3763–3768.
50 A. Bodi, B. Sztáray, T. Baer, M. Johnson and T. Gerber, *Rev. Sci. Instrum.*, 2007, **78**, 084102.
51 O. K. Rice and H. C. Ramsperger, *J. Am. Chem. Soc.*, 1927, **49**, 1617–1629.
52 O. K. Rice and H. C. Ramsperger, *J. Am. Chem. Soc.*, 1928, **50**, 617–620.
53 R. A. Marcus and O. K. Rice, *J. Phys. Chem.*, 1950, **55**, 894–908.
54 L. A. Curtiss, P. C. Redfern and K. Raghavachari, *J. Chem. Phys.*, 2007, **126**, 084108.
55 M. J. Frisch, G. W. Trucks, H. B. Schlegel, G. E. Scuseria, M. A. Robb, J. R. Cheeseman, G. Scalmani, V. Barone, B. Mennucci, G. A. Petersson, *et al.*, *Gaussian 16 Revision A.03*, Gaussian, Inc., Wallingford CT, 2016.
56 Y. Shao, L. F. Molnar, Y. Jung, J. Kussmann, C. Ochsenfeld, S. T. Brown, A. T. Gilbert, L. V. Slipchenko, S. V. Levchenko and D. P. O'Neill, *Phys. Chem. Chem. Phys.*, 2006, **8**, 3172–3191.
57 B. Yang, J. Wang, T. A. Cool, N. Hansen, S. Skeen and D. L. Osborn, *Int. J. Mass Spectrom.*, 2012, **309**, 118–128.
58 S. Gozem, A. O. Gunina, T. Ichino, D. L. Osborn, J. F. Stanton and A. I. Krylov, *J. Phys. Chem. Lett.*, 2015, **6**, 4532–4540.
59 A. Bodi, P. Hemberger and R. P. Tuckett, *Phys. Chem. Chem. Phys.*, 2017, **19**, 30173–30180.
60 A. Bodi, N. S. Shuman and T. Baer, *Phys. Chem. Chem. Phys.*, 2009, **11**, 11013–11021.
61 Y. L. Sergeev, M. E. Akopyan, F. I. Vilesov and Y. V. Chizhov, *High Energy Chem.*, 1973, **7**, 369.
62 J. Harvey, A. Bodi, R. P. Tuckett and B. Sztáray, *Phys. Chem. Chem. Phys.*, 2012, **14**, 3935–3948.
63 *NIST Chemistry WebBook, NIST Standard Reference Database Number 69*, ed. P. J. Linstrom and W. G. Mallard, National

Institute of Standards and Technology, Gaithersburg MD, http://webbook.nist.gov, accessed September 2019.
64 S. Borkar, B. Sztáray and A. Bodi, *Int. J. Mass Spectrom.*, 2012, **330**, 100–108.
65 J. Bouwman, B. L. Sztáray, J. Oomens, P. Hemberger and A. Bodi, *J. Phys. Chem. A*, 2015, **119**, 1127–1136.
66 G. Bouchoux, J.-Y. Salpin and M. Yáñez, *J. Phys. Chem. A*, 2004, **108**, 9853–9862.
67 C. Peng, P. Y. Ayala, H. B. Schlegel and M. J. Frisch, *J. Comput. Chem.*, 1996, **17**, 49–56.
68 W. Stevens, B. Sztáray, N. Shuman, T. Baer and J. Troe, *J. Phys. Chem. A*, 2008, **113**, 573–582.

